Microseismic Event Detection Kalman Filter: Derivation of the Noise Covariance Matrix and Automated First Break Determination for Accurate Source Location Estimation

Erick Baziw[1], Bohdan Nedilko[1], and Iain Weir-Jones[1]

Abstract — Since 1972, Weir-Jones Engineering Consultants (WJEC) has been involved in the development and installation of microseismic monitoring systems for the mining, heavy construction and oil/gas industries. To be of practical value in an industrial environment, microseismic monitoring systems must produce information which is both reliable and timely. The most critical parameters obtained from a microseismic monitoring system are the real-time location and magnitude of the seismic events. Location and magnitude are derived using source location algorithms that typically utilize forward modeling and iterative optimal estimation techniques to determine the location of the global minimum of a predefined cost function in a three-dimensional solution space. Generally, this cost function is defined as the RMS difference between measured seismic time series information and synthetic measurements generated by assuming a velocity structure for the area under investigation (forward modeling). The seismic data typically used in the source location algorithm includes *P*- and *S*-wave arrival times, and raypath angles of incidence obtained from *P*-wave hodogram analysis and *P*-wave first break identification. In order to obtain accurate and timely source location estimates it is of paramount importance that the extraction of accurate *P*-wave and *S*-wave information from the recorded time series be automated—in this way consistent data can be made available with minimal delay. WJEC has invested considerable resources in the development of real-time digital filters to optimize extraction, and this paper outlines some of the enhancements made to existing Kalman Filter designs to facilitate the automation of *P*-wave first break identification.

Key words: Microseismic monitoring, Kalman filter, discrete covariance matrix, state-space, seismic wavelet first break, hodograms.

1. Introduction

A microseismic monitoring system is an assembly of hardware and software components designed to acquire and analyze, in real time, the acoustic signals collected by an array of appropriate transducers. Systems are generally installed in areas where seismicity has been induced by human activity. Seismic activity is often observed in the vicinity of underground excavations, deep open pits and quarries,

---

[1] Weir-Jones Engineering Consultants Ltd., 2040 West 10th Ave., Vancouver, B.C. Canada, V6J 2B3. Fax: 604-732-4801. E-mail: wjgroup@weir-jones.com

around and below large reservoirs where fluids are being injected into, or removed from, permeable subsurface formations, and adjacent to the sites of large underground explosions (GIBOWICZ and KIJKO, 1994). In regions where the level of induced seismicity is high and it is accompanied by significant ambient noise, it is essential that the microseismic monitoring systems possess the capability of automatically identifying the *P* and *S* waves generated by seismic events within the noise contaminated raw seismic time series. Reliable automated identification allows for the timely analysis of a large volume of data and the delivery of results to the end user in a useful manner. The ability to locate microseismic events accurately is directly dependent upon the ability to identify the *P*- and *S*-wave responses (phase association) and determine subsequent arrival times (phase picking) (GE and KAISER, 1992).

The technical challenges associated with automated phase association and picking can be reduced if the raw data are of high quality. To this end the authors and their colleagues have developed a number of multi-element seismic sensor arrays with bandwidths, signal-to-noise ratios, and mechanical characteristics tailored to different seismic environments. In addition, much effort has been invested in formulating intelligent digital signal processing algorithms for real-time seismic event detection. BAZIW and WEIR-JONES (2002) present a detailed discussion of a Microseismic Event Detection Kalman Filter (MEDKF). In this paper, a thorough review of the Kalman filter formulation is provided along with the governing equations defining the MEDKF. In the original MEDKF formulation some modeling simplifications were assumed when deriving the *Noise Covariance Transition Matrix*. In Section 2 of this paper, the *Noise Covariance Matrix* is derived without the modeling simplifications and the new MEDKF governing equations are presented.

There are three fundamental time series measurements obtained from the installed seismic sensor array which allow the investigator to locate an event accurately. These parameters are:

- the angles of incidence obtained from hodogram or polarization analysis and *P*-wave first break identification,
- *P*- and *S*-wave arrival times,
- *P-S* arrival time differences.

Generally, source location algorithms attempt to minimize iteratively a cost function identified as the RMS difference between the three fundamental parameters and corresponding synthetic derived values. The derivation of synthetic values is referred to as forward modeling and this requires the specification of the velocity structure of the area under investigation. Section 3 elaborates on the importance of utilizing raypath angles of incidence measurements of appropriate precision so that an optimal and cost effective seismic sensor network is implemented while maintaining the required seismic event location accuracy. In Section 3 the ability of the MEDKF to automate the *P*-wave first break identification is also discussed. Finally, Section 4

outlines arrival time estimation results from a microseismic monitoring installation in Northern Alberta where cyclic steam stimulation is occurring.

2. Microseismic Event Detection Kalman Filter Formulation

The microseismic phase association and event picking digital signal processing filters designed and implemented by the authors rely upon real-time and time domain mathematical algorithms such as the Kalman filter. The Kalman filter is an optimal (in a least-squares sense) recursive filter which is based on state-space, time-domain formulation of physical problems. In this way it avoids the difficulties commonly associated with frequency domain filters (BAZIW, 1993), and is ideal for real-time applications. The filter requires that the physical problem be modeled by a set of first-order differential equations which, with initial conditions, uniquely define the system behavior. The filter utilizes a knowledge of system and measurement errors and statistical information about the initial conditions. A thorough discussion of the continuous, discrete, and nonlinear versions of the Kalman Filter is provided by BAZIW (1988) and BAZIW and WEIR-JONES (2002).

In general terms, The Kalman filter is a method for estimating a state vector $\underline{x}$ from measurement $\underline{z}$. The state vector may be corrupted by a noise vector $\underline{w}$ and the measurement vector is corrupted by a noise vector $\underline{v}$. The filter is applicable for systems that can be described by a first order differential equation in $\underline{x}$ and a linear (matrix) equation in $\underline{z}$. The filter can be described in both continuous and discrete form. The continuous state and measurement equations are given by

$$\dot{\underline{x}}(t) = F(t)\underline{x}(t) + G(t)\underline{w}(t) \tag{1}$$

$$\underline{z}(t) = H(t)\underline{x}(t) + \underline{v}(t), \tag{2}$$

where $\underline{x}$ is an n vector, $\underline{w}$ is a p vector, and $\underline{z}$ and $\underline{v}$ are m vectors. The random (vector) processes $\underline{w}$ and $\underline{v}$ are assumed to be zero mean, white noise processes. It is further assumed that $\underline{w}$ and $\underline{v}$ are statistically independent of each other. The corresponding discrete state and measurement equations are given by

$$\underline{x}_k = \Phi_{k-1}\underline{x}_{k-1} + \Gamma_{k-1}\underline{w}_{k-1}, \quad \underline{w}_k \approx N(\underline{0}, Q_k) \tag{3}$$

$$\underline{z}_k = H_k\underline{x}_k + \underline{v}_k, \quad \underline{v}_k \approx N(\underline{0}, R_k). \tag{4}$$

In equations (3) and (4), symbol N denotes a normal distribution with mean $\underline{0}$ and variance Q_k and R_k, respectively. In addition, Φ is defined as the *State Transition Matrix*, Γ is the *Input Transition Matrix*, and H is the *Measurement Matrix*. The discrete Kalman Filter estimation equations are outlined as follows:
State Estimate Extrapolation:

$$\hat{\underline{x}}_k(-) = \Phi_{k-1}\hat{\underline{x}}_{k-1}(+), \tag{5}$$

Error Covariance Extrapolation:

$$P_k(-) = \Phi_{k-1} P_{k-1}(+) \Phi_{k-1}^T + \Gamma_{k-1} Q_{k-1} \Gamma_{k-1}^T. \tag{6}$$

The term $\Gamma_{k-1} Q_{k-1} \Gamma_{k-1}^T$ in equation (6) is referred to as the *Noise Covariance Matrix* (NCM).

State Estimate Update:

$$\hat{\underline{x}}_k(+) = \hat{\underline{x}}_k(-) + K_k[\underline{z}_k - H_k \hat{\underline{x}}_k(-)] \tag{7}$$

Error Covariance Update:

$$P_k(+) = [\mathbf{I} - K_k H_k] P_k(-) \tag{8}$$

I is the identity matrix in equation (8).

Kalman Gain Matrix:

$$K_k = P_k(-) H_k^T \left[H_k P_k(-) H_k^T + R_k \right]^{-1} \tag{9}$$

Initial Conditions:

$$\mathrm{E}[\underline{x}_0] = \hat{\underline{x}}_0, \quad \mathrm{E}\left[(\underline{x}_0 - \hat{\underline{x}}_0)(\underline{x}_0 - \hat{\underline{x}}_0)^T\right] = P_0. \tag{10}$$

The computational sequence for the discrete Kalman filter is outlined as follows:

A. At time index $k = 0$, specify initial conditions $\hat{\underline{x}}_0$, and P_0, and compute Φ_0 and Q_0.

B. At time index $k = 1$, compute $\hat{\underline{x}}_1(-)$, $P_1(-)$, H_1, R_1, and the gain matrix K_1.

C. Using the measurement $\underline{z}_1$ at time index $k = 1$, the best estimate of the state at $k = 1$ is given by

$$\hat{x}_1(+) = \hat{x}_1(-) + K_1[z_1 - H_1 \hat{x}_1(-)].$$

D. Update the error covariance matrix $P_1(+)$.

E. At time index $k = 2$, a new measurement $\underline{z}_2$ is obtained and the computational cycle is repeated.

The MEDKF is a three state Kalman Filter incorporating ambient noise and seismic wavelet responses within the recorded time series (BAZIW and WEIR-JONES, 2002). The ambient noise is modeled as a Gauss-Markov process with the following continuous system representation:

$$\dot{n}(t) = -\beta\, n(t) + \sqrt{2\sigma^2\beta}\, w(t). \tag{11}$$

In equation (11) $\mathrm{E}[w(t)w(\tau)] = \delta(t-\tau)$, where $\delta(t-\tau)$ is the Dirac delta function, and σ^2 and T_c (i.e., $\beta = 1/T_c$) define the variance and time constant of the process. The discrete form of equation (11) is written as:

$$\begin{aligned} &n_{k+1} = a_w n_k + b_w w_k \\ &\text{where,}\quad a_w = e^{-\beta\Delta} \quad \text{and}\quad b_w = \sigma\sqrt{(1 - e^{-2\beta\Delta})}. \end{aligned} \tag{12}$$

In equation (12), w_k is a zero-mean, timewise-uncorrelated, unit-variance sequence with a Gaussian probability distribution function. n_k is therefore a zero-mean, exponentially-correlated random variable whose standard deviation is σ.

The seismic wavelet is modeled as a periodic process with a random walk amplitude. This process is defined as:

$$x_1(t) = x_2(t)\sin(\omega t). \qquad (13)$$

In equation (13), $x_1(t)$ is an approximation to the *P*-wave or *S*-wave seismic wavelet, and $x_2(t)$ is a random walk process approximating the exponentially decaying seismic wavelet amplitude. The random walk process facilitates the provision of some flexibility to the MEDKF when determining the arrival time and initial amplitude of the seismic wavelet under study. The random walk process results when uncorrelated signals are integrated. The process is defined as its derivative being driven by white noise as follows:

$$\dot{x}_2(t) = w(t), \quad \text{where} \quad \mathrm{E}[w(t)w(\tau)] = Q\delta(t - \tau). \qquad (14)$$

By using a random walk process to define the seismic wavelets amplitude, one is able to account for arrival time variations and maintain linearity in the KF formulation. The linear continuous differential equation defining the seismic wavelet is:

$$\dot{x}_1(t) = \omega x_2(t)\cos(\omega t) + \sin(\omega t)w(t) \qquad (15)$$

$$\dot{x}_2(t) = w(t), \quad \text{where} \quad \mathrm{E}[w(t)w(\tau)] = Q\delta(t - \tau). \qquad (16)$$

To simplify the formulation of the MEDKF governing equations, BAZIW and WEIR-JONES (2002) made the assumption that state $x_2(t)$ was considered to be constant when differentiating equation (14). In this paper, this assumption is no longer made and a slightly modified MEDKF formulation is obtained. The *State Transition Matrix* remains unaffected by relaxing the assumption that state $x_2(t)$ remains constant, however the *Input Transition Matrix* and the *Noise Covariance Matrix* change for the seismic wavelet model. From equations (11) and (15) the continuous MEDKF matrix system equation is defined as:

$$\begin{bmatrix} \dot{x}_1(t) \\ \dot{x}_2(t) \\ \dot{x}_3(t) \end{bmatrix} = \underbrace{\begin{bmatrix} 0 & \omega\cos(\omega t) & 0 \\ 0 & 0 & 0 \\ 0 & 0 & -\beta \end{bmatrix}}_{=F(t)} \begin{bmatrix} x_1(t) \\ x_2(t) \\ x_3(t) \end{bmatrix} + \underbrace{\begin{bmatrix} \sqrt{Q}\sin(\omega t) & 0 \\ \sqrt{Q} & 0 \\ 0 & \sqrt{2\sigma^2\beta} \end{bmatrix}}_{=G(t)} \begin{bmatrix} w_1(t) \\ w_2(t) \end{bmatrix}$$

$$(17)$$

In equation (17), $E[w_1(t)w_1(\tau)] = \delta(t - \tau)$ *and* $E[w_2(t)w_2(\tau)] = \delta(t - \tau)$. Both $w_1(t)$ and $w_2(t)$ are Gaussian white-noise processes with mean zero and unity variance. The only difference between the continuous system outlined in equation (17) and that presented by BAZIW and WEIR-JONES (2002) is the continuous *Input Transition Matrix* $G(t)$; therefore, the discrete *Transition Matrix* does not change with the
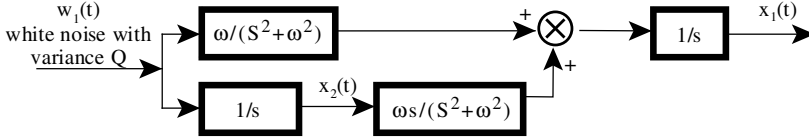
Figure 1
Periodic random walk process block diagram.

formulation defined in equation (17), however it is required to derive an updated discrete *Noise Covariance Matrix*.

Due to the fact that the ambient noise and seismic wavelet models are independent of one another, they can be treated separately. Figure 1 illustrates the block diagram of the seismic wavelet modeled as a random walk periodic process with the following transfer functions:

$$G'(w_1 \text{ to } x_1) = G'_1 = 2\omega/(s(s^2 + \omega^2)), \tag{18}$$

$$G'(w_1 \text{ to } x_2) = G'_2 = 1/s. \tag{19}$$

In equations (18) and (19) s is the Laplacian variable. The corresponding weighting functions are:

$$g'_1(t) = \frac{2}{\omega}[1 - \cos(\omega t)], \tag{20}$$

$$g'_2(t) = 1. \tag{21}$$

The *Noise Covariance Matrix* (NCM) can be determined by calculating the mean-square response (GELB, 1978) of $x_1(t)$ and $x_2(t)$ as follows:

$$\begin{aligned} NCM = \mathrm{E}[x_i x_j] &= \int_0^\Delta \int_0^\Delta g'_i g'_j \mathrm{E}[w_1(u)w_1(v)]\, du\, dv \\ &= \int_0^\Delta g'_i g'_j \delta(u-v) Q\, du\, dv. \end{aligned} \tag{22}$$

Carrying out the necessary calculations results in the following seismic wavelet *Noise Covariance Matrix*:

$$NCM = \frac{2Q}{\omega} \begin{bmatrix} \frac{2}{\omega}\left[\frac{3}{2}\Delta - \frac{2\sin(\omega\Delta)}{\omega} + \frac{\cos(\omega\Delta)\sin(\omega\Delta)}{2\omega}\right] & \left[\Delta - \frac{\sin(\omega\Delta)}{\omega}\right] \\ \left[\Delta - \frac{\sin(\omega\Delta)}{\omega}\right] & \frac{\Delta\omega}{2} \end{bmatrix}. \tag{23}$$

In equation (23) Δ is the sampling rate.

BAZIW and WEIR-JONES (2002) describe how the MEDKF's ambient noise model parameters are determined adaptively from the raw seismic time series by automatically

deriving the ambient noise autocorrelation automatically. From the ambient noise autocorrelation the variance (σ^2) and time constant ($1/\beta$) parameters are obtained adaptively. The random noise Q value is adaptively specified in a manner similar to the technique utilized by LEAR (1985) when modeling nondeterministic forces such as the acceleration of a fighter plane in a dog fight with another plane. In this case, the acceleration standard deviation is chosen to be about $1/3$ of the expected maximum acceleration. In specifying the Q value for the MEDKF, the algorithm identifies the maximum amplitude within the seismic time series under investigation and sets the Q value to $1/9$ of the square of this maximum. The initial state vector $\underline{x}_0$ is set to the null vector [0, 0, 0] and the initial error covariance matrix is set to null matrix except for the diagonal elements which are all set to Q.

3. Accurate Source Location Estimation Utilizing Automated First Breaks with the MEDKF

The primary objective of a microseismic investigation is to obtain accurate event locations from measured seismic time series in a timely manner. Generally, the seismic location algorithm utilizes forward modeling to generate synthetic measurements which are iteratively compared to actual measurements. The source location algorithm optimally minimizes a cost function based upon the L_1 or L_2 norm applied to differences between the measured and synthesized P- and S-wave arrival times, and angle of incidences determined from the P-wave particle motion. Inclusion of all these parameters in the cost function increases the source location accuracy and subsequently decreases the solution space.

P-wave hodogram or polarization analysis is carried out to determine the incident angles of the seismic source raypath. In this methodology, it is very important to obtain accurate P-wave first break estimates so that reliable incident angle measurements are derived. In the case of a linear array of transducers, the azimuth angle information derived from the hodogram analysis allows the investigator to limit the solution space to the event's azimuth plane and subsequently reduce the source location problem from three dimensions to two dimensions (i.e., range and depth on azimuth plane).

In passive seismic monitoring the event time is not available as an input parameter; therefore, the investigator is required to compare relative sensor arrival times. The time differencing of P-wave arrival times in microseismic event location results in hyperbolic solution spaces. The intersection of the azimuth, P-wave time differencing, and P-S wave time separation solution spaces serves as an estimate of source location error.

The MEDKF has been configured so that it not only automates the estimation of the P-wave and S-wave arrival times, but it also gives first break information for the raypath angles of incidence determination.
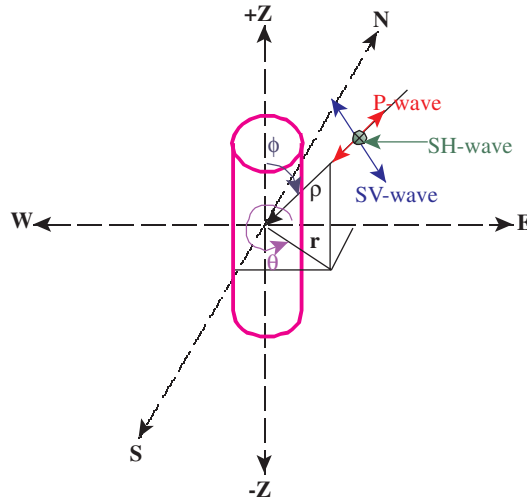
Figure 2
Source *P*, *SV*, and *SH* wavelets impacting on seismic sensor.

3.1 Deriving Incidence Angles from P-wave Hodogram Analysis

Figure 2 illustrates the compression (*P*) and shear (*SV* and *SH*) source wavelets impacting upon a seismic sensor package. As it is shown in Figure 2, the *P*-wave's particle motion is in the same direction as the raypath, the *SH* wavelet's particle motion is perpendicular to the raypath and is parallel to the horizontal ground surface, and the SV wavelet's particle motion is also perpendicular to the raypath but along the vertical normal to the raypath. The symbols ϕ and θ define the raypath's angles of incidence in spherical coordinates, where $0 \leq \theta \leq 360°$ and $0 \leq \phi \leq 180°$. The investigator carries out hodogram analysis to derive the angles of incidence of the source wavelet arriving at the sondes.

The hodogram analysis procedure starts by specifying a time window which delineates the *P* wave for the *E*, *N*, and *Z* component seismic sensors in a triaxial package configuration. An example of a time window identifying the *P*-wave pulse is illustrated in Figure 3(a) where the time windows are marked with thicker lines. The amplitudes of *E*, *N*, and *Z* component seismic time series are plotted against one another (hodograms) within the time window. A least-squares regression line is then applied to the hodograms. Slopes of the three lines $tg(\Theta_{yx})$, $tg(\Theta_{yz})$, and $tg(\Theta_{xz})$ provide angle of incidence information, which is then corrected with respect to direction of the wavelet arrival. Figure 3(b) illustrates the hodograms with regression lines drawn.

Finally, a covariance matrix is calculated for the hodograms. The eigenvalues of this covariance matrix allow for linearity calculations. Highly accurate hodograms
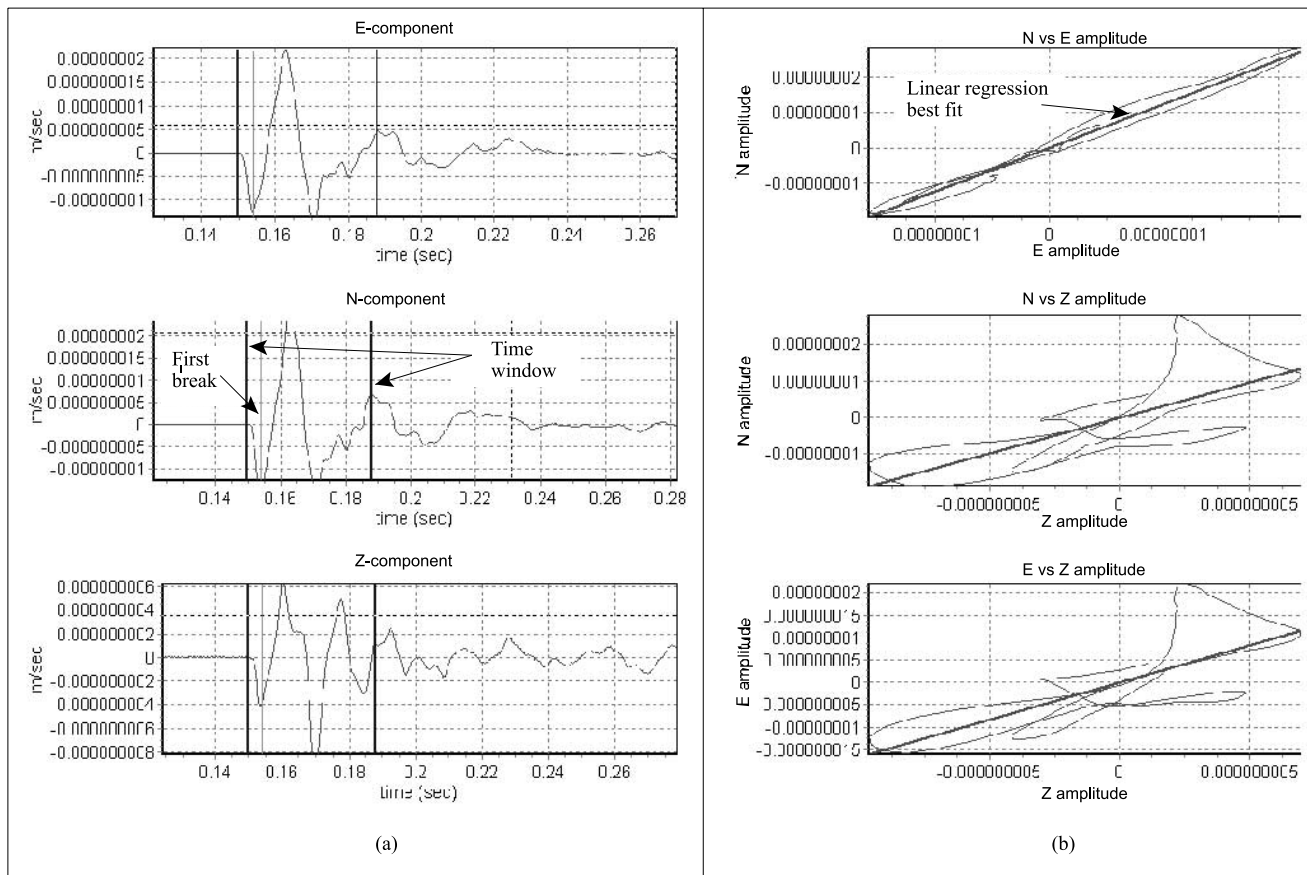
Figure 3
Windowing on seismic wavelets (a) and 3-D hodograms (b).

have a linearity approaching 1.0 and low accuracy hodograms have a linearity near zero.

The angles ϕ and θ obtained from the hodogram analysis will range from $-90°$ to $+90°$. *P*-wave first break arrival time information allows the investigator to convert these so that $0° \leq \theta \leq 360°$, and $0° \leq \phi \leq 180°$. The direction of the seismic sensor particle motions is derived from the signs of *E*, *N*, and *Z* components of the seismic time series at the arrival time.

The derived hodogram angles are converted to global incident angles by defining the incident angles of the seismic ray as the angle which would be required to give the proper signs of the *E*, *N*, and *Z* component amplitudes at the first break arrival time. For example, in the *E-N* plane, if the first break arrival time is indicative of negative *E* and *N* component responses, then the incident ray is assumed to reside in the first quadrant. In the case of multiple linear arrays, the azimuth solution space is calculated as an intersection of lines which delineate the azimuth angle tolerances. Figure 4 illustrates the plane view of the solution space for two linear arrays. If only one linear array is available for analysis, the width of the uncertainty or error of the azimuth plane estimate can be used as a delineator for the azimuth solution space.

3.2 Obtaining Microseismic Locations in Homogeneous Medium Utilizing P-wave and S-wave Time Differencing

As previously stated, the final solution space is derived by the intersections of the *P*-wave incident angle solution space, the *P*-wave hyperbolic solution space,
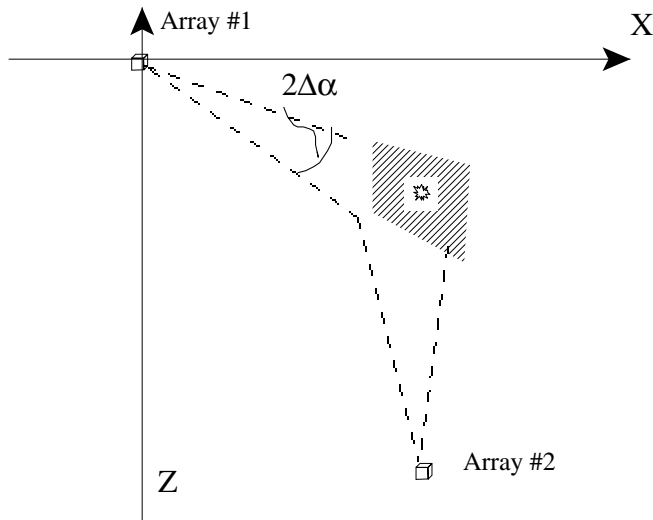

Figure 4
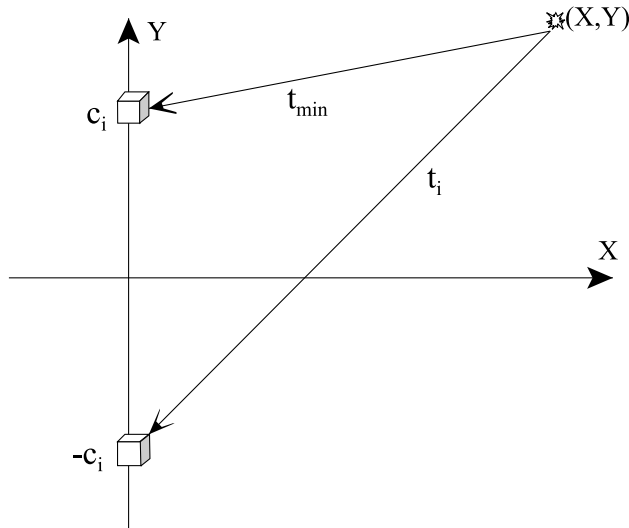Azimuth solution space is formed by four intersecting tolerance lines (plan view).

Figure 5
Simplified time differencing model.

and the *P-S* wave arrival time separation solution space. The time differencing of *P*-wave arrival times in microseismic event location results in hyperbolic solution spaces. The principle of arrival-time differencing is outlined by considering the two sensors illustrated in Figure 5. A seismic event location is calculated using the differences of arrival times detected at the two sondes. This approach has been used in shore-based marine radio navigation systems (e.g., shoran and the rho-rho mode of Loran-C), and is applicable to microseismic event location (GE and HARDY, 1988).

To simplify the model, we assume a constant *P*-wave velocity, V_p, along the source-sensor raypath. If the vertical axis of the azimuth plane is positioned along the sensors' vertical array, and the *X*-axis is centered between the two sondes, then the time differencing equation for *i*th sensor is defined as:

$$\sqrt{x^2 + (c_0 - y)^2} - \sqrt{x^2 + (c_i + y)^2} = V_p(t_i - t_{\min}). \qquad (24)$$

In equation (24), $t_{\min}$ is the minimal arrival time for the array, x and y are the source coordinates on the azimuth plane, and t_i is the arrival time at the *i*th sensor.

The standard equation which defines a hyperbola is given as:

$$\frac{y^2}{b^2} - \frac{x^2}{a^2} = 1. \qquad (25)$$

Equation (24) is fitted into the format of equation (25) by letting y_i be the vertical coordinate of ith transducer, and y_{min} be the coordinate of the triggering transducer. Then:

$$a_i^2 = \frac{4c_i^2 - s_i^2}{4}, \tag{26}$$

$$b_i^2 = \frac{s_i^2}{4}, \tag{27}$$

where

$$c_i = \left| \frac{y_i - y_{min}}{2} \right|, \tag{28}$$

$$s_i = V_p(t_i - t_{min}) = V_p \Delta t_i, \tag{29}$$

$$\Delta t_i = t_i - t_{min}. \tag{30}$$

Substituting the a_i and b_i parameters defined in equations (26) and (27) into (25), results in the set of hyperbolae shown in Figure 6 (i.e., $y = \pm\sqrt{\left(1 + \frac{x^2}{a_i^2}\right)b_i^2}$).

A minimum of two time difference measurements is required in order to obtain a source location on the azimuth plane. Generally, there will be inherent arrival time detection errors, δt_i, that result in perturbations of the hyperbolae as illustrated in Figure 7. The arrival time errors lead to a non-unique microseismic event location with a solution space defined by the overlapped perturbed hyperbolae. When Δt_i is substituted in equation (29) by $\Delta t_i \pm \delta t_i$, we obtain a_i', b_i', a_i'', and b_i'' which define upper and lower limits of the perturbed area.
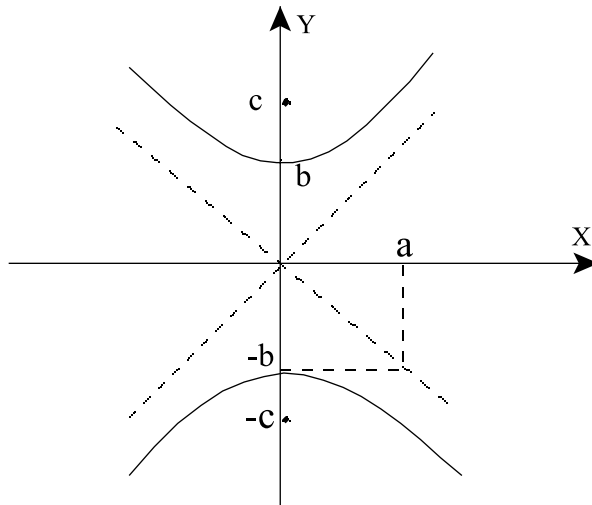

Figure 6
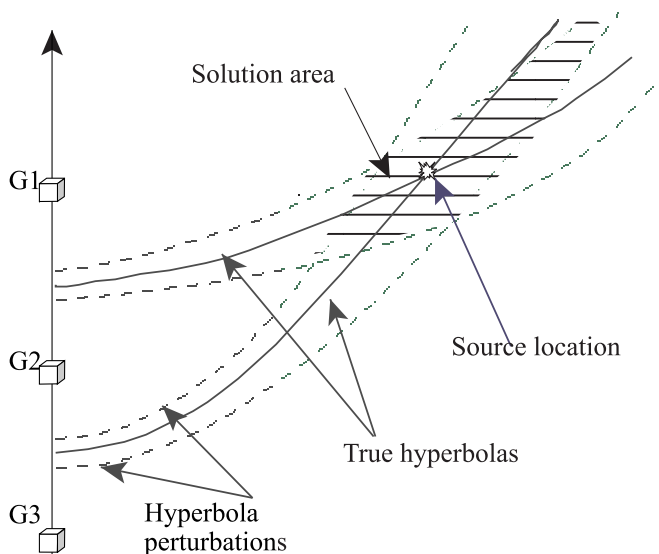The principle of *P*-wave arrival time difference produces two hyperbolas for each pair of geophones.

Figure 7
If errors are present in arrival time data, the solution area is formed by overlapped tolerance intervals.

The solution space can be reduced in size by adding more seismic sensors to the network (i.e., increasing the density of the time difference hyperbolas) and by strategically placing them around the area under microseismic investigation. Alternatively, the investigator can incorporate measured *P-S* time differences in the source location algorithm so that the solution space can be further reduced.

The time difference between *P* wave and *S* wave originating from the same seismic event defines a sphere with its origin at the recording sensor and radius at the source location. On the azimuth plane, this sphere becomes a circle with radius R_i. centered at the *i*th recording sensor.

If we assume constant *P-S* velocities along the raypath, then for the *i*th geophone we have:

$$V_p t_i = V_s(t_i + \Delta t_i^{p-s}), \tag{31}$$

where t_i is the time it takes a *P* wave to travel from the source of the seismic event to a geophone, and Δt_i^{p-s} is the *P-S* arrival time difference. If we let R_i be the distance between a source and the *i*th geophone then:

$$R_i = V_p t_i \tag{32}$$

and

$$\Delta t_i^{p-s} = \frac{R_i}{V_s} - \frac{R_i}{V_p}, \tag{33}$$

from equation (31) it follows that:

$$t_i = \frac{\Delta t_i V_s}{V_p - V_s}.$$ (34)

When an investigator applies the principle of *P-S* arrival time to calculate a source location, only the measurement Δt_i^{p-s} rather than t_i is available. If an error δt_i^{p-s} is present in the measurements of Δt_i^{p-s}, tolerances for the *P-S* arrival time difference solution space are calculated as:

$$R_i^{1,2} = \frac{V_p V_s}{V_p - V_s}(\Delta t_i^{p-s} \pm \delta t_i^{p-s})$$ (35)

which follows from equations. (32) and (34).

Equation (35) produces two confocal circles as is illustrated in Figure 8. The reduced solution space resulting from the incorporation of the *P*-wave arrival time differences, Figure 7, and the *P-S* time difference solution space, Figure 8, is illustrated in Figure 9. The final solution space which is defined as the intersection of the azimuth (for a single linear array), *P*-wave time differencing, and *P-S* wave time separation solution spaces is shown in Figure 10.

3.3 Utilizing the MEDKF for First Break Estimation

As outlined in Section 2 and discussed by BAZIW and WEIR-JONES (2002), the MEDKF models the seismic source wavelet as a random walk periodic process as a best approximation to an exponentially decaying cyclic waveform which is defined as
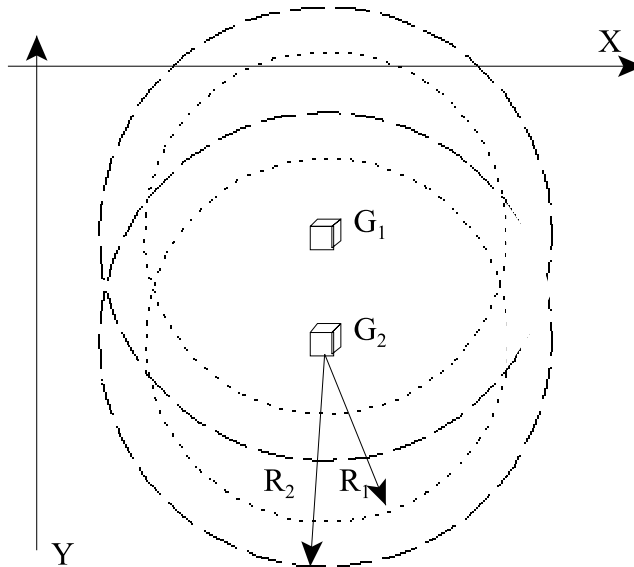

Figure 8
Microseismic solution space utilizing *P-S* time differencing for two vertical sondes.
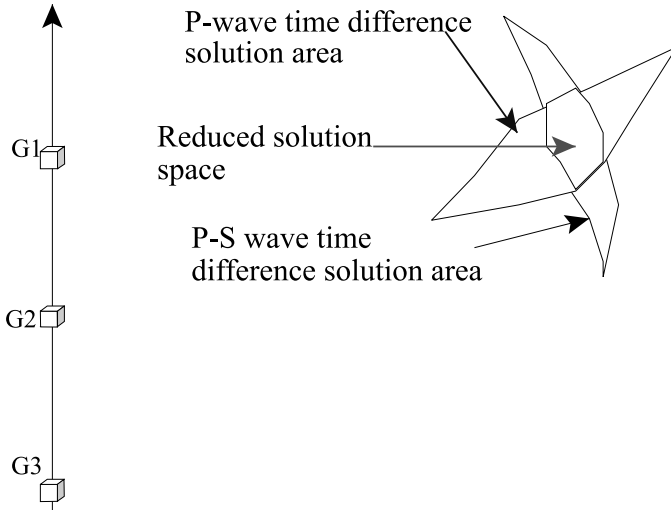
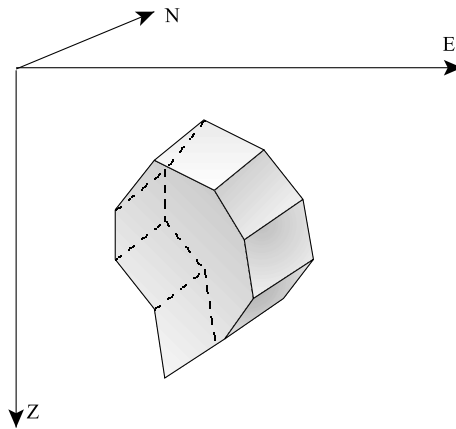Figure 9
Illustration of reduced solution space.

Figure 10
Final solution space for a linear seismic array. The solution space is defined as intersection of the azimuth, *P*-wave time differencing, and *P-S* wave time separation solution spaces.

$$A(t) = A_0 e^{-h(t-t_0)} \sin\left[\omega(t - t_0)\right], \quad t \geq t_0. \tag{36}$$

In equation (36) $A_0 \equiv$ initial amplitude, $h \equiv$ damping factor, $t_0 \equiv$ wavelet arrival time, and $\omega \equiv$ dominant angular frequency (i.e., $\omega = 2\pi f$). The filter tracks the random walk state (x_2) which is a best estimate of the term $A_0 e^{-h(t-t0)}$ in equation (37).

The state x_2 approximates the amplitude of the source wavelet, and its maximum value within the time series depends upon whether the source wavelet is minimum, mixed, or maximum phase; for these reasons, it is not possible to determine the first break arrival time based solely on the maximum response of the x_2 state. The technique implemented by the authors to automate the first break source wavelet detection is to track the full seismic waveform amplitude defined as:

$$\rho(t)_{\text{MEDKF}} = \sqrt{E(t)^2_{\text{MEDKF}-x_2} + N(t)^2_{\text{MEDKF}-x_2} + Z(t)^2_{\text{MEDKF}-x_2}}, \qquad (37)$$

where $\rho(t)_{\text{MEDKF}}$ defines the MEDKF full seismic waveform amplitude time series derived from the MEDKF x_2 best estimates of the *E*ast, *N*orth, and *Z* component time series. The time location of the maximum $\rho(t)_{\text{MEDKF}}$ amplitude response reflects the condition of the wavelet under study (i.e., whether it is minimum, mixed, or maximum phased). To obtain the first break arrival time, the user needs to determine the initial rise time of $\rho(t)_{\text{MEDKF}}$ due to the input of the source wavelet under study. This is accomplished by moving back from the maximum $\rho(t)_{\text{MEDKF}}$ value within the time series until a time index is identified where the $\rho(t_{\text{first break}})_{\text{MEDKF}}$ amplitude is within 10% to 20% of the maximum $\rho(t)_{\text{MEDKF}}$ amplitude. This time index is identified as the first break arrival time.

4. Results

The data presented in this paper were obtained from a microseismic installation Weir-Jones. Engineering Consultants had commissioned at heavy oil extraction operations in Northern Alberta. Earlier work in this region has been described by other authors (TALEBI *et al.*, 1998).

The Cold Lake area is located in Northern Alberta, Canada. Extensive, heavy oil reserves underlie the area. The oil sands occur in the Mannville Group of Lower Cretaceous age and range from 305 m to 610 m below surface. The primary reservoir is the Clearwater formation at an average depth of 457 m. The sand in the Clearwater is laterally and vertically continuous and pay thickness ranges from 15 m to 49 m. The reservoir has 11 billion m^3 of bitumen in place.

The Clearwater sand is an unconsolidated clean sand with porosities between 30% and 35% and an average bitumen saturation of 70%. The absolute permeability ranges from 0.5×10^{-12} m^2 to 2×10^{-12} m^2 and viscosity reaches 150,000 cp. Initial reservoir conditions are 3 °C and 3 MPa. Figure 11 illustrates a typical steam injection mechanism where there is pancake stratigraphy which is defined as follows:

Overlying the Clearwater formation is the Grand Rapids formation, which consists of sands and shales. Above this is the Colorado Group of Upper Cretaceous age. It consists of marine shales that are impervious and separate the oil sands from the glacial tills near surface. Since most of the oil sands are immobile, additional heat

Table 1

Cold Lake Pancake Stratigraphic Formations

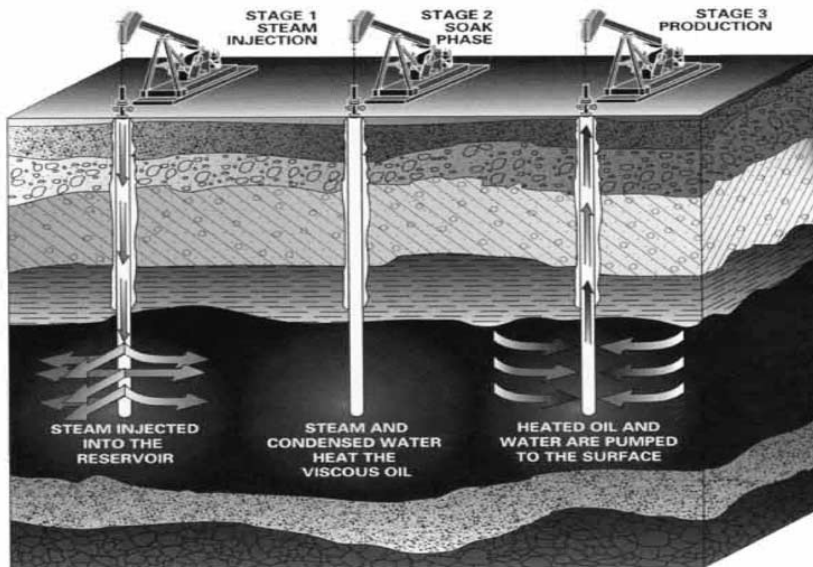| Formation Top	Depth(m)
Surface	0
Colorado Shales	149
Grand Rapids	319
Clearwater	432
McMurray	485

Figure 11
Typical steam injection mechanism in Northen Alberta.

and pressure are required to recover the bitumen. Three main processes used are cyclic steam stimulation, steam drive and steam assisted gravity drainage. A detailed technical description of the microseismic monitoring equipment and geophone sondes installation was presented by TALEBI (1998).

The data analyzed in this paper were obtained using proprietary geophone arrays specifically developed by the authors for these applications. The geophone arrays consist of multiple sensing elements arranged on orthogonal axes. The arrays have a natural frequency of 10 Hz, are damped at 70% of critical, and have a bandwidth from 15 to 600 Hz.The seismic data analyzed in this section were acquired with a linear array of five triaxial multi-element geophones. The geophones are located at
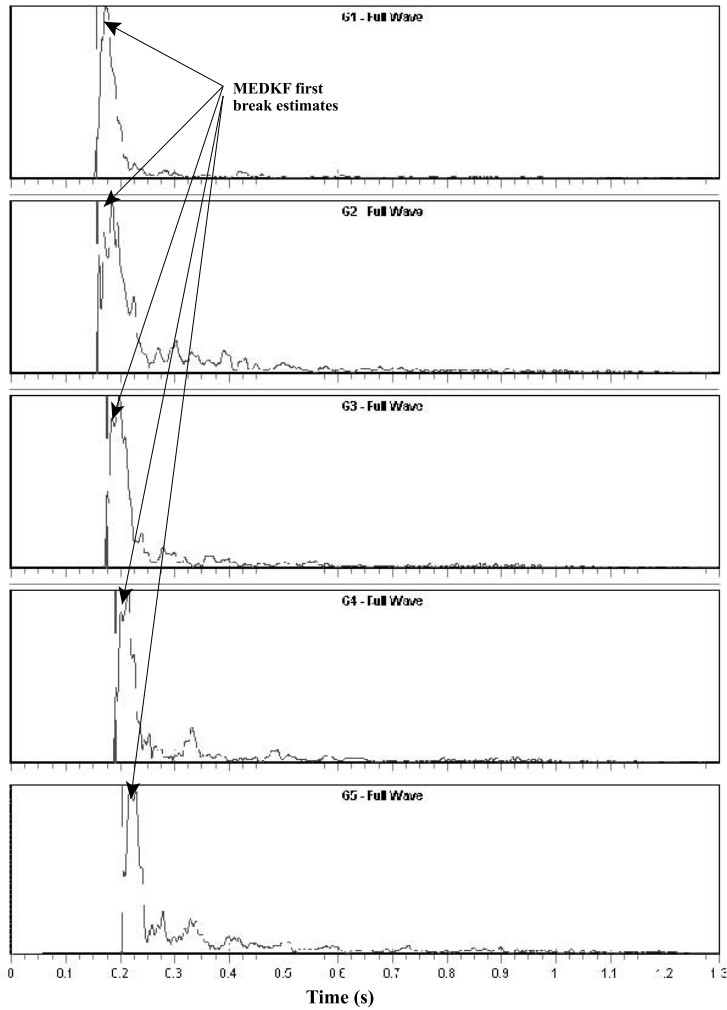
Time (s)
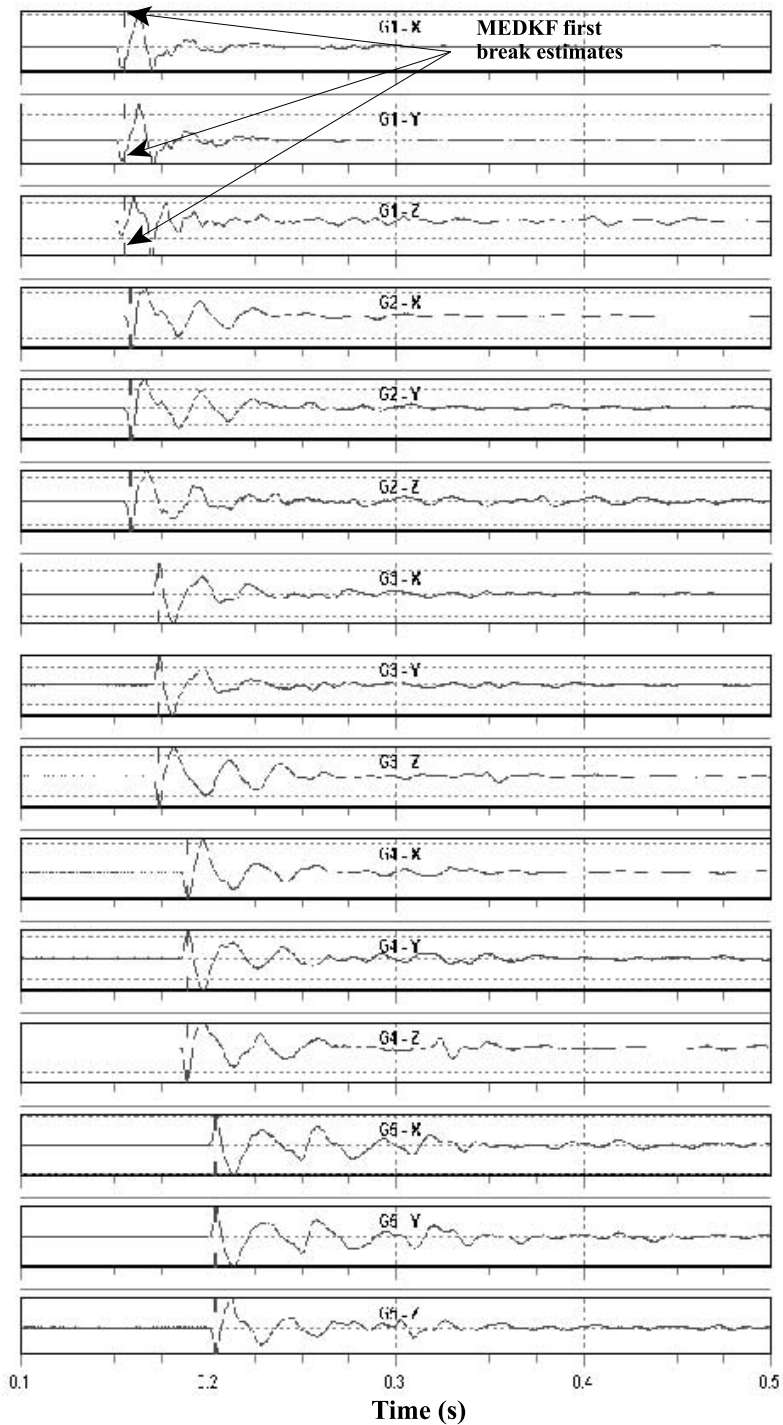
Figure 13
The MEDKF's full waveform state x_2 estimates resulting from the input illustrated in Figure 13. The vertical lines identify the MEDKF's first break estimates.

approximate depths of m 155 m (G1), 215 m (G2), 280 m (G3), 340 m (G4), and 400 m (G5).

For the Cold Lake area, the velocity model utilized in the forward modeling portion of the source location algorithm is defined as follows:

◄

Figure 12
Seismic time series responses from a linear five component triaxial multi-element geophase array due to sensor orientation calibration shot. The vertical lines identify the MEDKF's first break estimates.

Table 2

Cold Lake Two Layer Velocity Model

Layer	Elevation	*P*-wave velocity	*S*-wave velocity
Top	0.0 m to 325 m	2000 m/sec	660 m/sec
Bottom	> 325 m	2200 m/sec	1000 m/sec

Figure 12 shows the seismic time series plots obtained from the previously described linear five component triaxial geophone array whose orientation is being derived from a calibration shot. Figure 13 illustrates the corresponding $\rho(t)_{MEDKF}$ time series estimates. The first break arrival times are determined by moving back from the maximum values within the $\rho(t)_{MEDKF}$ time series until the $\rho(t_{first\ break})_{MEDKF}$ amplitudes are within 20% of the maximum $\rho(t)_{MEDKF}$ amplitudes. The accurately estimated MEDKF automated first break arrival times are shown in Figures 12 and 13 by vertical lines.

Figure 14 illustrates the time series from the linear array sondes generated by a microseismic event occurring on 14th July, 10:05:17. The G1 sonde responses have been omitted because they only contained ambient noise. Figure 15 illustrates the MEDKF full waveform estimates for the first breaks of the *P*-wave phases while Figure 16 shows the MEDKF full waveform arrival time estimates for the *S*-wave phases. The MEDKF *P*-wave filter dominant frequency was set to 290 Hz with a ±100 Hz frequency tolerance, while the MEDKF *S*-wave filter dominant frequency was set to 60 Hz with a ±60 frequency tolerance. The frequency tolerance parameter allows for the MEDKF to take into account source signal frequency attenuation as the wavelet travels to each sonde.

Figure 17 shows the 14th July, 10:05:17 microseismic event time series with the accurate MEDKF estimated *P*-wave and *S*-wave first break estimates superimposed. Based upon the MEDKF *P*-wave first break estimates and carrying out automated hodogram analysis, the optimal estimate of the source azimuth plane is N 80° E with a root-mean-square (RMS) error of 2°. The source location is calculated to be 69 m east, 12 m north, and 400 m in depth with an overall RMS positional error on the azimuth plane of 2.0 m.

Figure 18 illustrates the solution space *P*-wave time difference hyperbolas and *P*-*S*-wave time separation solution spaces based upon the arrival times illustrated in Figure 17. The optimal source location is also superimposed onto Figure 18 where the source range is calculated to be 70 m. As is shown in Figure 18, the source location estimate resides within the cluster of intersections of the *P*-wave hyperbolas

▶

Figure 14

Acquired seismic time series from the linear array sondes generated by the microseismic event of 23rd May, 13:58:11.
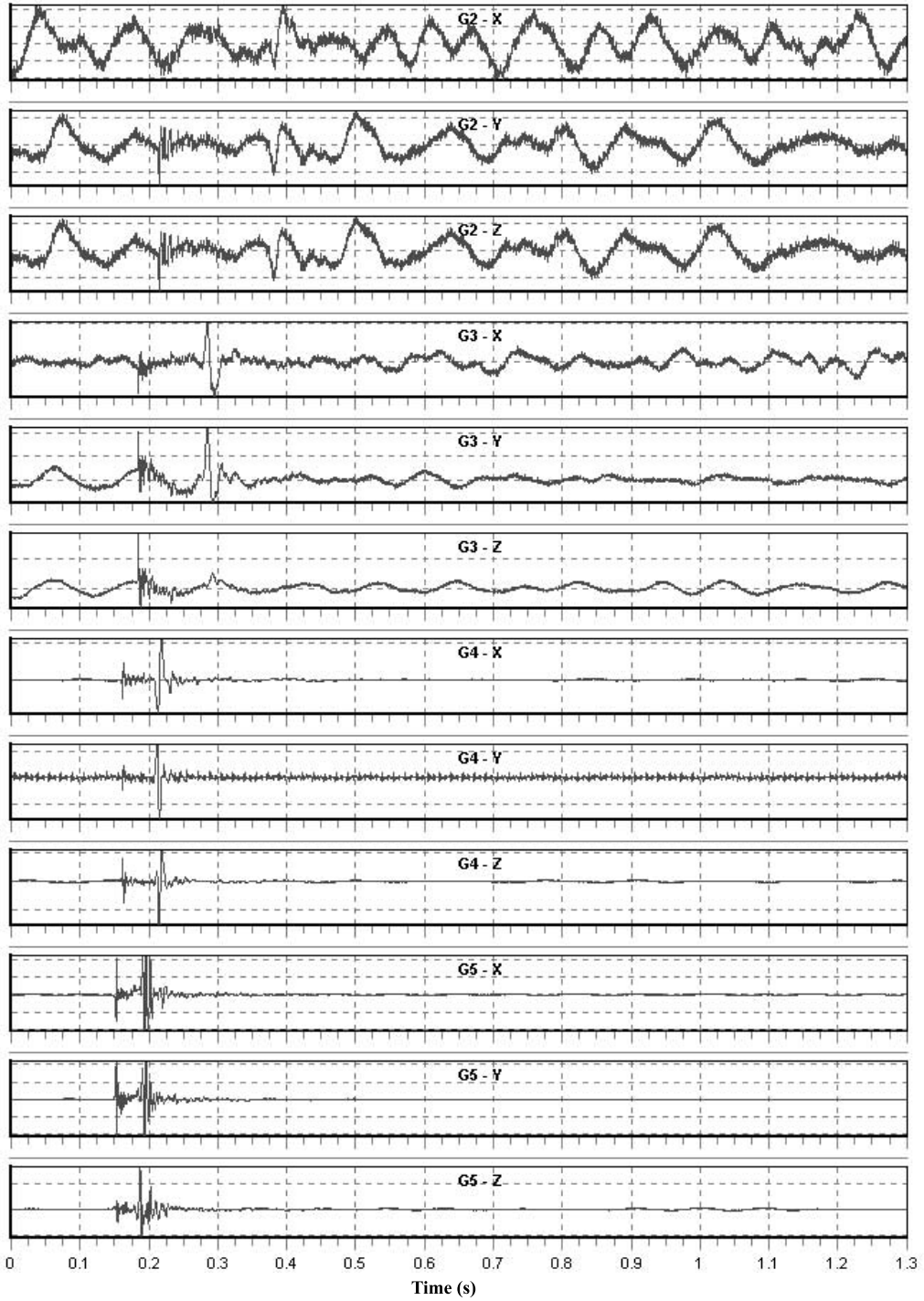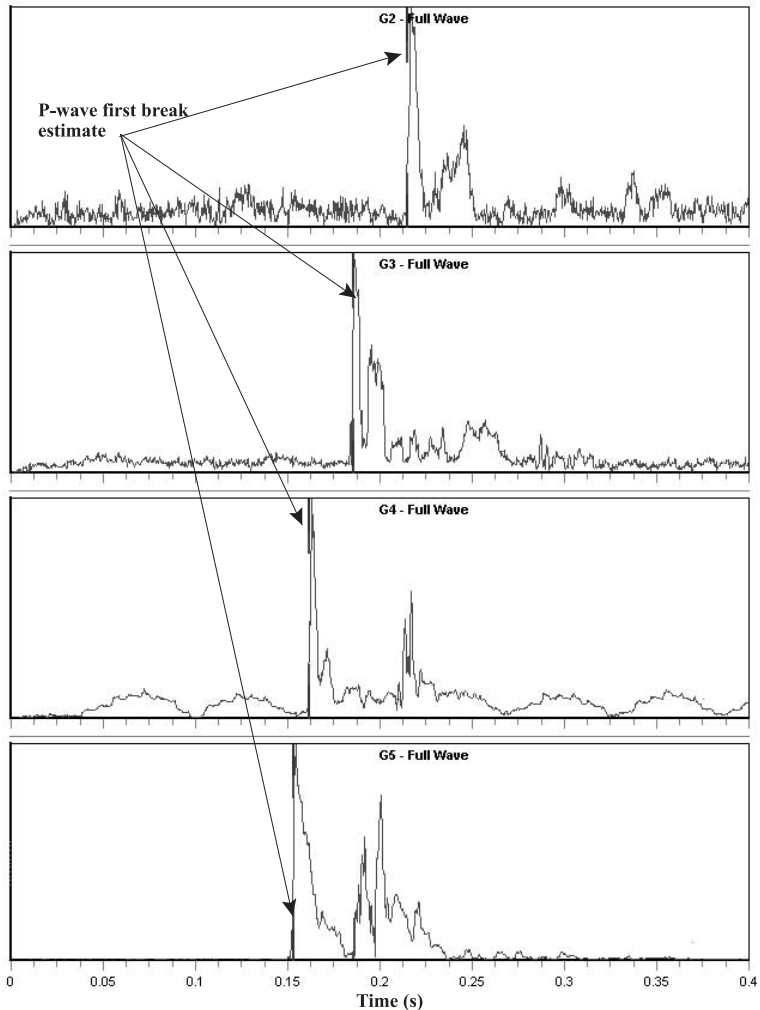
Time (s)

Figure 15
MEDKF's estimated *P*-wave full waveform first break estimated from the input illustrated in Figure 15.

and the *P-S* wave arrival time separation solution spaces within the microseismic source azimuth plane. Figure 19 shows an expanded view of Figure 18. Figures 18 and 19 demonstrate that there is an excellent correlation between the derived hyperbolas and *P-S* wave arrival time separation solution spaces. Simplistically, the correlations indicate that there is an extremely high probability that the source lies at

▶

Figure 16
MEDKF's estimated S-wave full waveform first break estimated from the input illustrated in Figure 15.

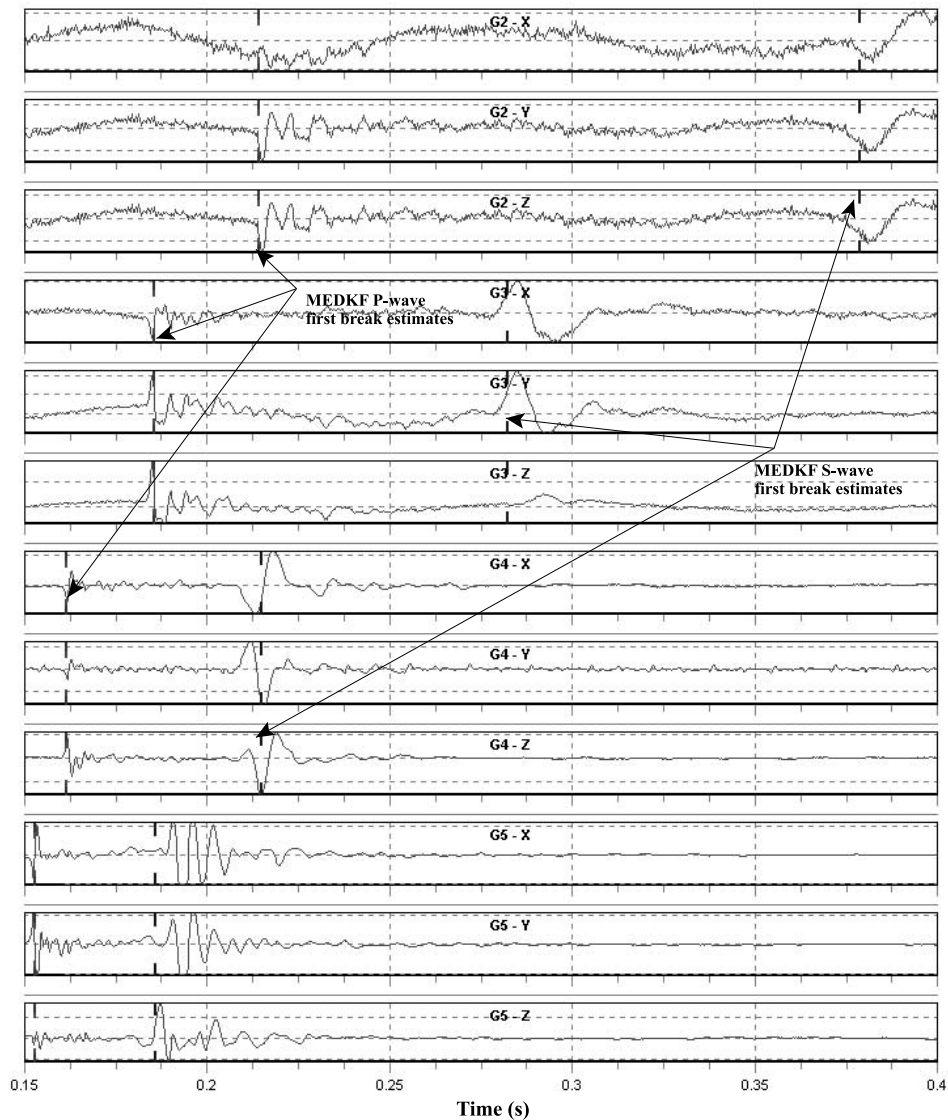**S-wave first break estimate**
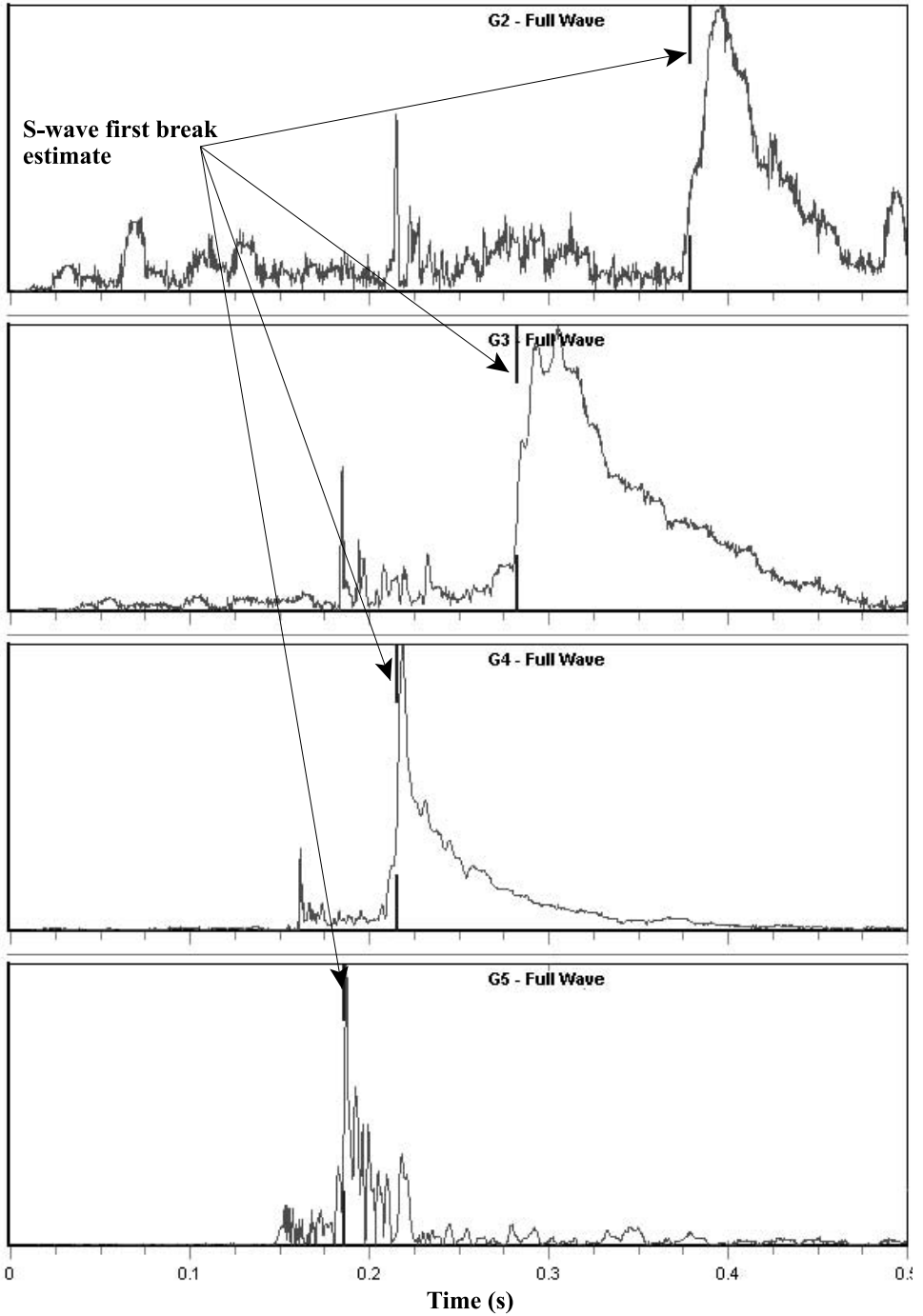
Figure 17

14th July 10:05:17 microseismic event *P*-wave and *S*-wave first break estimates based upon results illustrated in Figures 16 and 17.

a depth of between 395 m and 400 m and is between 70 m and 75 m from the borehole on a bearing of N 80° E.
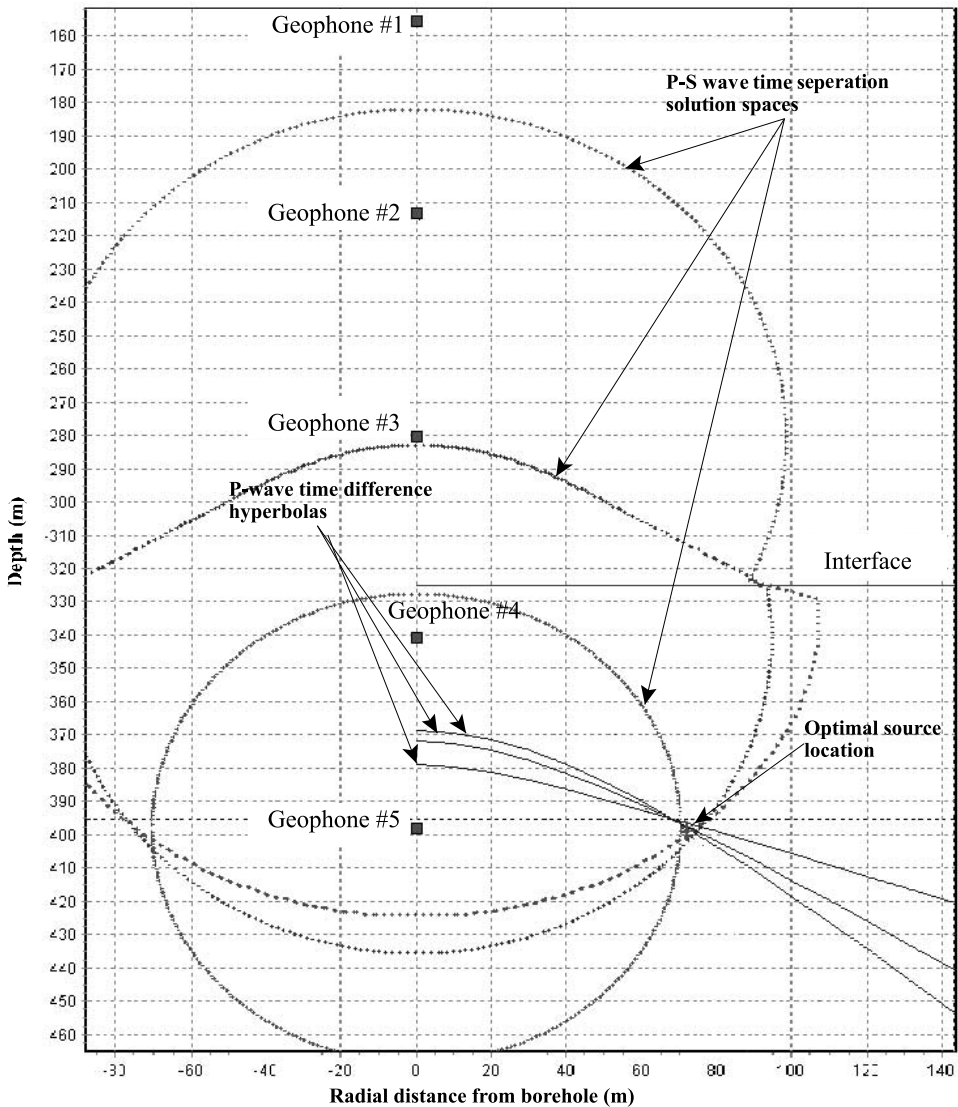
Figure 18
Illustration of the *P*-wave arrival time difference hyperbolas and *P-S* wave arrival time separation spaces for the 14th July, 10:05:17 microseismic event. Shown on the source azimuth plane bearing N 80° E.

4. Conclusions

The principle purpose of most microseismic monitoring systems is to provide reliable estimates of the real time location of the seismic events. In highly seismically active areas with significant ambient noise present, it is of paramount importance that microseismic monitoring systems have the capability of automating the
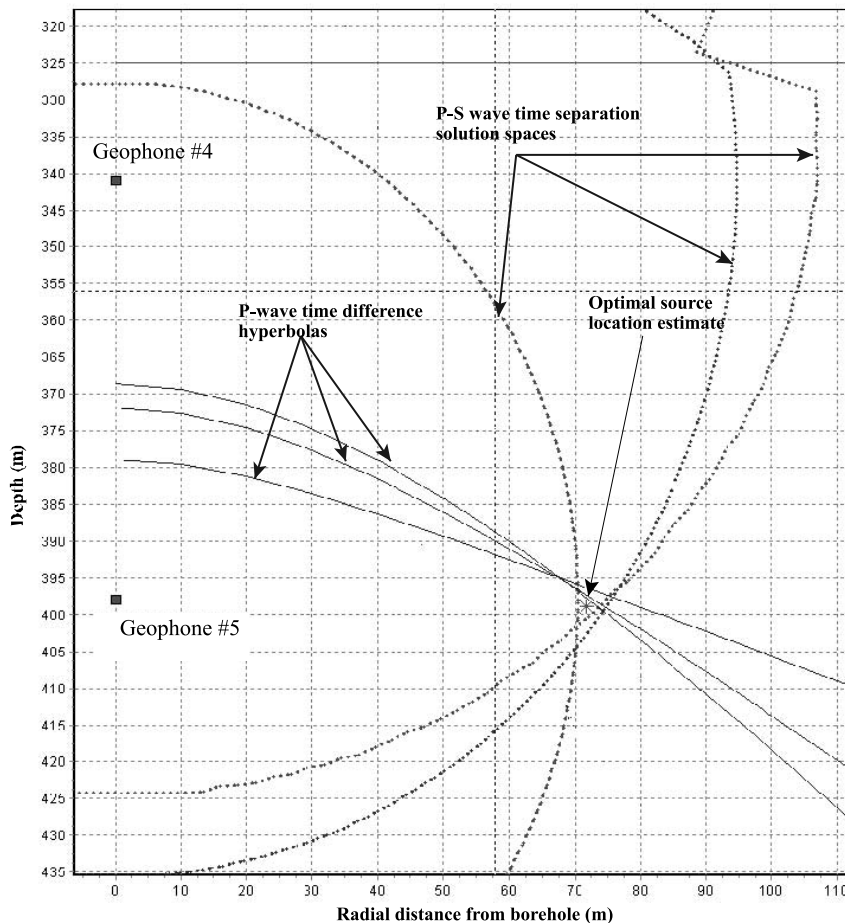
Figure 19
Enlargement of source area shown in Figure 18.

identification of *P*-wave and *S*-wave seismic events within the noise contaminated raw seismic time series. This allows for the timely analysis of large volumes of data. The ability to locate accurately microseismic events is directly dependent upon the ability to identify the *P*-wave and *S*-wave responses (phase association) and determine subsequent arrival times (phase picking).

These data are utilized in the microseismic source location algorithms which typically implement forward modeling and iterative optimal estimation techniques in which a global minimum of a predefined cost function is determined within the three-dimensional solution space. This paper has summarized some of the mathematical improvements being made to current microseismic event detection Kalman Filter

design and the ability to automate *P*-wave first break identification so that the event location solution space is kept to a minimum.

The ultimate objective is to provide reliable analytical procedures which will enable microseismic monitoring systems to be routinely used in production situations. Once this is achieved, operators will have available a tool which will enhance both safety and the cost effectiveness of many production processes.

REFERENCES

BAZIW, E.J. and WEIR-JONES, I. (2002), *Application of Kalman Filtering Techniques for Microseismic Event Detection*, Pure Appl. Geophys. *159*, 449–473.

BAZIW, E.J. (1993), *Digital Filtering Techniques for Interpreting Seismic Cone Data*, ASCE J. Geotech. Engin. *119* (6), 998–1018.

BAZIW, E.J. (1988), *Applications of Digital Filtering Techniques for Reducing and Analysing In Situ Seismic Time Series*, MASc Thesis, Dept. Of Civil Engineering, University of British Columbia, Vancouver, BC.

GELB, A., *Applied Optimal Estimation* (4th Edition, MIT Press, Cambridge, Mass. 1978).

GE, M. and KAISER, P. K. (1992), *Interpretation of Physical Status of Arrival Picks for Microseismic Source Location*, Bull. Seismol. Soc. Am. *80*, 1643–1660.

GE, M. and HARDY, H. R., Jr. (1988), *The Mechanism of Array Geometry in the Control of AE/MS Source Location Accuracy*, Proc. 29th U.S. Symposium on Rock Mechanics, Minneapolis, MN, 597–605.

GIBOWICZ, S.J. and KIJKO, A., *An Introduction to Mining Seismology* (Academic Press, 1994).

LEAR, W.M., *Kalman Filtering Techniques* (National Aeronautics and Space Administration Publication, Mission Planning and Analysis Division, No. JSC-20688 1985), 172–176.

TALEBI, S., NECHTSCHEIN, S., and BOONE, T.J. (1998), *Seismicity and Casing Failures Due to Steam Stimulation in Oil Sands*, Pure Appl. Geophys. *153*, 219–233.

To access this journal online:
http://www.birkhauser.ch